

# Cation–Anion Regulation Engineering in a Flame-Retardant Electrolyte toward Safe Na-Ion Batteries with Appealing Stability

Yi-Hu Feng, Chengye Lin, Hanwen Qin, Guang-Xu Wei, Chao Yang, Yongwei Tang, Xu Zhu, Shuai Sun, Tian-Ling Chen, Mengting Liu,\* Hong Zheng,\* Xiao Ji,\* Ya You, and Peng-Fei Wang\*



Cite This: <https://doi.org/10.1021/jacs.4c18326>



Read Online

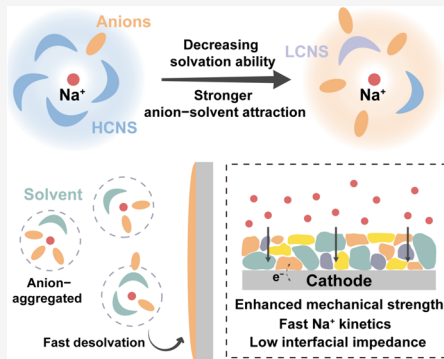
ACCESS |

Metrics & More

Article Recommendations

Supporting Information

**ABSTRACT:** Great electrochemical stability and intrinsic safety are of critical significance in realizing large-scale applications of Na-ion batteries (NIBs). Unfortunately, the notorious decomposition of the electrolyte and undesirable side reactions on the cathode–electrolyte interphase (CEI) pose major obstacles to the practical implementation of NIBs. Besides, the flammability of traditional carbonate-based electrolytes raises increasing safety concerns about the batteries. Herein, a flame-retardant all-fluorinated electrolyte is proposed to achieve an anion-aggregated inner solvation shell by modulating cation–anion interactions through a low-coordination number cosolvent. The more electrochemically antioxidant fluorinated solvents and anion-dominated interfacial chemistry contribute to the construction of both mechanically and chemically stable F-rich CEI. Such thin, homogeneous interphase effectively inhibits the parasitic reaction, strengthens the interfacial stability, and enables fast  $\text{Na}^+$  diffusion kinetics on the interface. When employing this electrolyte, the  $\text{Na}_{0.95}\text{Ni}_{0.4}\text{Fe}_{0.15}\text{Mn}_{0.3}\text{Ti}_{0.15}\text{O}_2$  (NFMT) cathode delivers remarkable discharge capacity up to  $169.7 \text{ mAh g}^{-1}$ , with stable cycling at 1C for 500 cycles. Impressively, NFMT//hard carbon pouch cells with such electrolyte also achieve a steady operation for 100 cycles at 0.5C with 86.8% capacity remaining. This study offers a practical reference for developing high-performance and flame-retardant electrolytes.



## INTRODUCTION

High-energy-density, cost-effective, and stable rechargeable battery technology is highly desired to meet the expanding needs of a sustainable society and the growing demand for renewable energy. Na-ion batteries (NIBs) are deemed to be a promising candidate for large-scale energy storage systems owing to their abundant resources, environmental friendliness, cost-efficiency, and similar mechanisms as Li-ion batteries (LIBs).<sup>1–6</sup> However, there are still gaps in specific energy density between advanced NIBs and LIBs, which dramatically obstruct their wide-scale application.<sup>7,8</sup> Nowadays, substantial progress has been achieved in researching high-capacity cathodes for NIBs capable of withstanding high voltages.<sup>9–13</sup> Unfortunately, the formation of a deteriorated cathode/electrolyte interphase (CEI) remains a critical challenge as a result of the uncontrollable side reaction and electrolyte decomposition under high-voltage conditions. Such unstable interphase leads to continuous depletion of electrolytes and structure degradation, eventually endowing capacity decay and posing a critical obstacle to the development of high-performance NIBs.<sup>14–18</sup> In addition, safety concerns of batteries are paramount, with the electrolyte being a primary cause of fire in batteries during thermal runaway, overcharging, and shock. The conventional solvents used in NIBs, typically carbonate and ether, are highly flammable and hazardous.<sup>19–22</sup>

These issues have become bottlenecks in the commercial development of NIBs, seriously limiting their full-scale application.

Given their unique physical and chemical properties, fluorinated electrolytes have gained wide attention in conquering the above-mentioned problems. Benefiting from the strong electronegativity of F, the fluorinated solvents are difficult to lose electrons, exhibiting excellent oxidation resistance at high voltages.<sup>23</sup> Meanwhile, endowed by the steric hindrance of fluorine atoms, fluorinated solvents show weaker solvation strength with cations, lowering the desolvation energy barrier.<sup>24–26</sup> The F atoms in the molecules deliver strong attractions to hydrogen radicals, effectively quenching the chain reaction in combustion, thus mitigating risks of thermal runaway.<sup>27–29</sup> Therefore, in recent years, the concept of all-fluorinated electrolytes has been applied in sodium batteries.<sup>30</sup> However, current research is mainly devoted to solid-state batteries, Na–S batteries, and Na–metal batteries.<sup>31–34</sup>

Received: December 21, 2024

Revised: April 24, 2025

Accepted: April 25, 2025

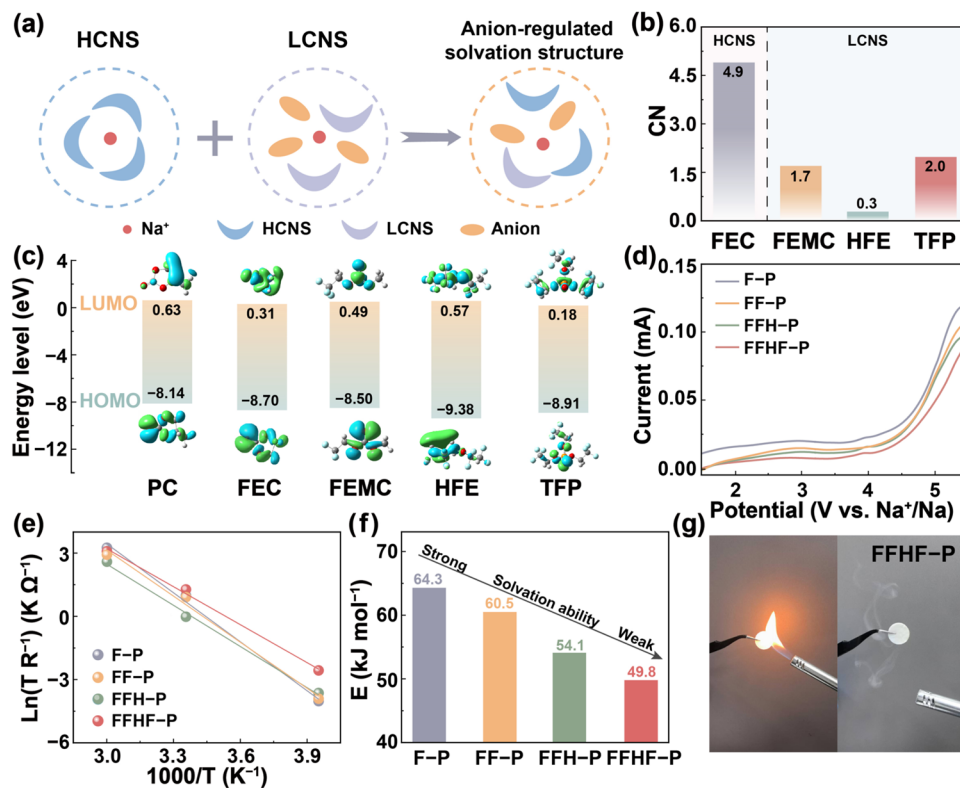


**Figure 1.** (a) Schematic diagram of the design strategy. (b) CN of FEC, FEMC, HFE, and TFP. (c) HOMO and LUMO energy levels of different solvents. (d) LSV results in fluorinated electrolytes. (e) Fitted Arrhenius plots and (f) the corresponding  $\text{Na}^+$  desolvation energy barrier of different electrolytes. (g) Flammability tests for the FFHF-P electrolyte.

Although some progress has been achieved, reports on their application in NIBs are still scarce, and their potential remains underexplored, thereby restricting their practical implementation. Meanwhile, many fluorinated molecules with weak solvation ability show low salt solubility, and unstable CEI with low ionic conductivity is often ineffective against severe parasitic reactions on the electrode, which further hinders the utilization of all-fluorinated electrolytes in NIBs. Aiming at improving the interfacial stability between electrolyte and electrode, strategies such as high-concentration electrolytes, localized high-concentration electrolytes, and weakly solvating electrolytes have been proposed to extend battery life by increasing the inorganic component in the electrode/electrolyte interphase via raising the proportion of anions in the solvation structure, efficiently stabilizing the electrode.<sup>28,35–38</sup> Nevertheless, their inherent drawbacks of high salt usage and limited solvent choices bring much uncertainty and are unfavorable for industrial applications. Recent reports have pointed out that when a certain amount of low-coordination number solvents (LCNS) is introduced into high-coordination number solvents (HCNS), the anions will be dragged into the  $\text{Na}^+$  solvation sheath due to the insufficient coordination of solvent molecules, which allows for anion-induced ion–solvent coordination structure at low salt concentration.<sup>39–41</sup> In this regard, designing a high-voltage fluorinated electrolyte that integrates flame retardancy and stable film-forming functionality through ion interaction regulation is essential for optimizing the performance of NIBs. Moreover, interactions within the fluorinated electrolyte also require urgent exploration, which is essential for progressing the fundamental principle of electrolyte engineering.

To address the above challenges, this work proposed a cation–anion interaction regulation strategy to design an all-fluorinated electrolyte with superior physicochemical characteristics by employing  $\text{NaPF}_6$ , fluoroethylene carbonate (FEC), methyl 2,2,2-trifluoroethyl ester (FEMC), 1,1,2,2-tetrafluoroethyl-2,2,3,3-tetrafluoropropylether (HFE), and tris(2,2,2-trifluoroethyl) phosphate (TFP). The addition of fluorine-containing LCNS to FEC strongly enhances the interactions between  $\text{Na}^+$  and anions, achieving a stable anion-induced solvation structure at a low salt concentration and facilitating rapid desolvation of  $\text{Na}^+$ . As a result, a thin, robust, and homogeneous anion-induced F-rich electrode/electrolyte interphase is constructed on the cathode, which can effectively suppress the parasitic reactions and reduce the interfacial transport barriers, thus enhancing the stability of the CEI and  $\text{Na}^+$  transport kinetics. Besides, the designed electrolyte imparts great flame-retardant properties, contributing to the safety of NIBs. The  $\text{Na}_{0.95}\text{Ni}_{0.4}\text{Fe}_{0.15}\text{Mn}_{0.3}\text{Ti}_{0.15}\text{O}_2$  (NFMT) // Na batteries employing such an electrolyte exhibit a high discharge capacity of over  $169 \text{ mAh g}^{-1}$  with long-term cycling stability for 500 cycles at a 1C rate. Moreover, the NFMT // hard carbon (HC) pouch cells deliver stable cycling performance and exhibit high capacity retention of 86.8% after 100 cycles at 0.5C. This work provides insights into the rational electrolyte design for safe and high-performance NIBs and demonstrates the feasibility of this strategy in addressing critical electrolyte challenges in practical applications.

## RESULTS AND DISCUSSION

As a typical fluorinated solvent, FEC delivers great sodium salt solubility and high coordination number (CN), which allows

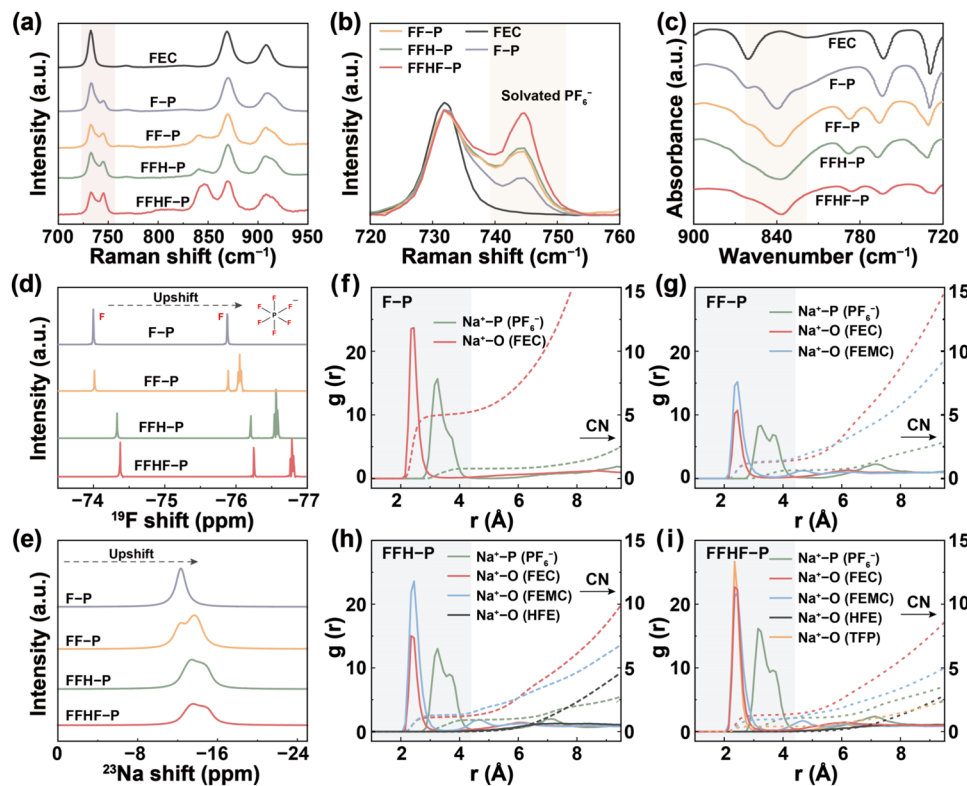


**Figure 2.** (a, b) Raman spectra of electrolytes with various combinations. (c) FTIR profiles of different electrolytes. (d)  $^{19}\text{F}$  NMR spectra of  $\text{PF}_6^-$  and (e)  $^{23}\text{Na}$  spectra of  $\text{Na}^+$  in selected electrolytes. (f–i)  $\text{Na}^+$  RDFs and CN in F-P, FF-P, FFH-P, and FFHF-P.

the establishment of a stable cation–dipole coupling structure. It is well recognized that such HCNS with strong polarities can effectively dissociate the Na salts and form a stable high-coordination structure with  $\text{Na}^+$ , thus excluding the anion from the solvation sheath.<sup>41</sup> Unfortunately, such cation–solvent clusters tend to make the desolvation process difficult and induce unstable CEI on the cathode, adversely affecting the long-term operation of batteries. LCNS usually exhibit weak coordination with cations, which facilitates the generation of anion-induced interphase. However, they often suffer from poor conductivity and undesirable solubility and cannot be applied as a sole solvent in electrolytes. With this understanding, when LCNS is introduced into HCNS as a coordinated diluent, the  $\text{Na}^+$  fails to be sufficiently coordinated with solvent molecules, and the incomplete coordination induces extensive participation of anions in the solvated sheath, allowing the formation of anion-induced solvated structure even in HCNS (Figure 1a). The newly designed nonflammable electrolyte consists of 1 M  $\text{NaPF}_6$  dissolved in FEC/FEMC/HFE/TFP (1:1:1:1 in volume ratio), abbreviated as FFHF-P. For comparison, electrolytes with different solvents (denoted as F-P, FF-P, and FFH-P) and the common propylene carbonate (PC)-based electrolyte (denoted as PC-P) were also prepared. The specific components of all electrolytes are listed in Table S1.

To verify the coordination ability of selected solvents, the CN of FEC, FEMC, HFE, and TFP were calculated by molecular dynamics (MD) simulations when the concentration of  $\text{NaPF}_6$  is fixed as 1 M. As shown in Figures 1b and S1, the CN of FEC is 4.9, indicating a high coordination strength with  $\text{Na}^+$ . Instead, the values of FEMC, HFE, and TFP are only 1.7, 0.3, and 2.0, respectively, and thus, they are categorized as LCNS. The highest occupied molecular orbital (HOMO) and

lowest unoccupied molecular orbital (LUMO) energy levels of solvents were obtained by density functional theory (DFT) calculation (Figure 1c). Due to the strong electron-withdrawing effect of the F, the F-containing solvents are difficult to be oxidized and show low HOMO energy levels, thus ensuring enhanced oxidation resistance. To experimentally verify the above design principles, the electrochemical oxidative stability of different electrolytes was assessed by linear sweep voltammetry (LSV) tests. As shown in Figures 1d and S2, all curves act as straight baselines, and the oxidation onset voltages of fluorinated electrolytes are much higher than that of conventional PC-P, indicating that the fluorinated substituents with a strong electron-withdrawing effect effectively widen the electrochemical window. When the potential is scanned to 4.0 V, a strong oxidation current appears in F-P, reflecting the decomposition at high voltage. Further, with the addition of FEMC, HFE, and TFP, the cutoff voltage of FFHF-P appeared at higher voltages, which is attributed to the lower HOMO energy levels. Meanwhile, the weaker solvation effect leads to an increase in the anion content in the solvation structure. The abundant ion pairing in the system effectively stabilizes the electrons in the anions, reducing the ability of anions to lose electrons. Thus, the designed electrolyte demonstrates enhanced antioxidant capability and shows potential for high-voltage applications. Moreover, the current at low potentials should also be considered, as it plays a dominant role in the stability of the cells and the formation of the electrode/electrolyte interphase.<sup>42</sup> As a result, FFHF-P provides the smallest current in the low-voltage region, implying less decomposition during cycling.

The energy barriers for  $\text{Na}^+$  desolvation ( $E$ ) were obtained according to the Arrhenius equation based on the temperature-

related electrochemical impedance spectroscopy (EIS), as depicted in Figures 1e,f and S3. Compared to other electrolytes, FFHF-P possesses the lowest  $E$ , implying less difficulty in the desolvation process and facilitating the fast transport of  $\text{Na}^+$  through the surface. Such optimization reveals the enhanced transport ability restricted by the coordination of solvent molecules, which contributes to lowering interfacial reaction polarization, thus enabling better performance at a high rate. These advantages are all related to the weak solvation around  $\text{Na}^+$  and the special solvation structure with anion aggregation in FFHF-P, which will be further discussed below. Flammability tests were conducted to verify the safety characteristics of the electrolyte, as outlined in Figures 1g, S4, and S5. The separator immersed with conventional PC-P electrolyte, which is generally considered highly flammable, ignited instantly and burned vigorously upon contact with the flame. The F-P electrolyte was also combusted after prolonged exposure to fire. Conversely, the FFHF-P electrolyte is not supportive of combustion at all, performing superior nonflammability. Such superior flame resistance is attributed to the fluorinated design for resisting burning, as strong attractions of F to H atoms contribute to inhibiting chain reactions during combustion.

When Na salt is dissolved in the solvents, the  $\text{Na}^+$  and anions dissociate first, followed by the competition between the anion and solvent molecules for coordination with  $\text{Na}^+$  in the electrolyte. Thus, differences in the solvent–salt interaction would strongly affect the coordination of  $\text{PF}_6^-$  anions in the solvation structures. The  $\text{Na}^+$  and  $\text{PF}_6^-$  coordination behavior in the electrolyte was first characterized by Raman spectra, as presented in Figures 2a,b, S6, and S7. The vibration peaks at 731.6, 868.7, and 909.0  $\text{cm}^{-1}$  are detected for the pure FEC solvent. After the addition of  $\text{NaPF}_6$ , the extra peak at 915.1  $\text{cm}^{-1}$  represents the solvated FEC, indicating coordination between  $\text{Na}^+$  and FEC molecules. In parallel, a new peak located at 743.4  $\text{cm}^{-1}$  occurs, which is characteristic of the P–F stretching in coordinated  $\text{PF}_6^-$ , implying the crowding of  $\text{PF}_6^-$  into the  $\text{Na}^+$  solvation sheath.<sup>43</sup> Upon the introduction of LCNS, the peak belonging to solvated FEC is slightly weakened, while the Raman peak representing coordinated  $\text{PF}_6^-$  strengthens significantly. Such evolutions are mainly ascribed to the partial replacement of FEC by the LCNS, resulting in a poorer solvation ability and promoting more anions into the solvation sheath even at low salt concentrations. In the FFHF-P, the peak intensity around 743  $\text{cm}^{-1}$  immensely increases, confirming that more anions have successfully entered the solvation sheath of  $\text{Na}^+$ , contributing to the construction of anion-aggregation solvation structures. The variation of the solvation environment around  $\text{Na}^+$  and the coordination state of the anions in diverse electrolytes were also investigated by Fourier transform infrared spectroscopy (FTIR). The engagement state of  $\text{PF}_6^-$  can be determined in the active absorption band located at 920–800  $\text{cm}^{-1}$ , as manifested in Figures 2c and S8. The absorption peak located at 835  $\text{cm}^{-1}$  represents the uncoordinated symmetric  $\text{PF}_6^-$  (P–F vibration), suggesting its presence in the solvent-separated ion pairs (SSIP), while the contact ion pairs (CIPs) can be recognized via two wide bands at 864–856 and 823–828  $\text{cm}^{-1}$ .<sup>28,44</sup> Apparently, the proportion of CIPs in electrolytes containing LCNS is much higher than that in F-P electrolytes, proving that more  $\text{PF}_6^-$  are involved in the solvation shield and influence the coordination state of  $\text{Na}^+$ .

A more in-depth analysis concerning the effect of HCNS and LCNS on the  $\text{Na}^+$  solvation structure was performed using the nuclear magnetic resonance (NMR) technique. Figure 2d presents the  $^{19}\text{F}$  NMR spectra of fluorinated electrolytes with different solvents. In the electrolytes with pure FEC and  $\text{NaPF}_6$ ,  $\text{PF}_6^-$  can get rid of the restriction of the  $\text{Na}^+$  solvation environment to a maximum degree as more anions are present in the free state. As a result, the  $^{19}\text{F}$  signal of P–F in  $\text{PF}_6^-$  takes an obvious downfield position.<sup>45</sup> Such signals indicate that F–P fails to form an anion-aggregated solvation structure, which explains its poor electrochemical performance. Clearly, a large upfield shift of  $^{19}\text{F}$  peaks in the  $\text{NaPF}_6^-$  can be observed when the electrolyte changes from F-P to FF-P, FFH-P, and FFHF-P, implying the increased electron cloud density and enhanced shielding effect.<sup>28,46</sup> The conclusion is also supported by the  $^{23}\text{Na}$  NMR spectra (Figure 2e). Compared with F-P, the upfield shift of the  $^{23}\text{Na}$  NMR signal after adding LCNS is indicative of increased electron density around  $\text{Na}^+$ , demonstrating the intensive  $\text{PF}_6^-$  shielding effect on  $\text{Na}^+$ . In parallel, the line width of the NMR peak is broadened, implying more complex interactions and more aggregated solvation structure in the systems.<sup>47,48</sup> These outcomes prove the stronger interaction between  $\text{Na}^+$  and  $\text{PF}_6^-$  and demonstrate that the strategy of mixing LCNS and HCNS remodels the intermolecular interaction, promoting the transition from SSIP to CIPs and aggregates (AGGs), in agreement with the results obtained by Raman and FTIR. To conclude, the spectral analysis illustrates the existence of more  $\text{Na}^+$ –anionic structures in designed FFHF-P, which contributes to the formation of stable anion-induced CEI. Moreover, the participation of anions leads to a decrease in the solubility degree of Na salts, reducing the energy required for complete dissociation of  $\text{NaPF}_6$ , thus favoring the desolvation kinetics of  $\text{Na}^+$  and protection of CEI from being solubilized.<sup>47,49</sup>

MD simulations were performed to gain deeper insights into the interactions in the electrolytes and to provide information on the solvation structure of  $\text{Na}^+$  in more detail. The calculated radial distribution function (RDF) and corresponding CN of  $\text{Na}^+$ –coordination pairs in F-P, FF-P, FFH-P, and FFHF-P are presented in Figure 2f–i. The appearance of  $\text{Na}^+–\text{O}$  and  $\text{Na}^+–\text{P}$  peaks suggests that the solvent and  $\text{PF}_6^-$  anions are both involved in the first solvation sheath of  $\text{Na}^+$ . In the F-P electrolyte, it exhibits the highest CN of FEC (4.97) and the lowest CN of anions (0.78), denoting that FEC dominates the solvation structure. That is due to the strong solvation ability of FEC as HCNS, and the  $\text{Na}^+$  are well solvated, promoting the formation of SSIP. In contrast,  $\text{Na}^+$ –solvent and  $\text{Na}^+$ – $\text{PF}_6^-$  interactions showed opposite trends in each electrolyte system when the LCNS was introduced, indicating that the mix of HCNS and LCNS effectively reduces the overall coordination capability of electrolyte, which is conducive to facilitating the entry of anions into the solvation shell. As a result, the coordination environment changes considerably in FFHF-P. The interaction between FEC and  $\text{Na}^+$  is significantly weakened, as evidenced by the decrease in the CN of  $\text{Na}^+–\text{O}$  (FEC) to 1.28. Notably, the LCNS, although entering the solvation inner shell, still maintains a low CN, thus reducing the coordination ability of the electrolyte. In FFHF-P, the CNs of  $\text{Na}^+–\text{O}$  (FEMC),  $\text{Na}^+–\text{O}$  (HFE), and  $\text{Na}^+–\text{O}$  (TFP) are 0.96, 0, and 0.4, respectively. Such values are lower than the CNs when these LCNS serve as the sole solvents in the electrolytes (Figure S1), suggesting that LCNS exist as competitive coordinators in the system. The total CN of all

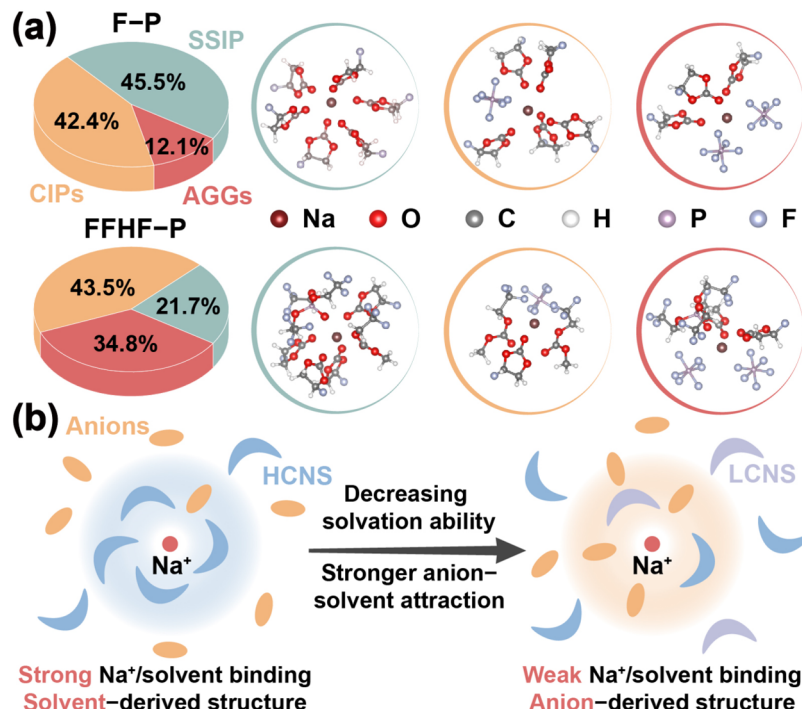


**Figure 3.** (a) Proportion of SSIP, CIPs, and AGGs in F-P and FFHF-P. (b) Schematic illustration of the formation of the anion-induced solvation structure.

solvents in FFHF-P is only 2.64, significantly lower than that of 4.97 in F-P, while the CN of Na<sup>+</sup>-P (PF<sub>6</sub><sup>-</sup>) increases sharply to 1.09. This implies that the anion-dominated solvation structure has been successfully established, and the NaPF<sub>6</sub> dissociates poorly in the system, benefiting the generation of large ionic aggregates like CIPs and AGGs. As a further step, details of the coordination environment in different fluorinated electrolytes were also calculated. According to the three defined solvated structures of SSIP, CIPs, and AGGs, the number of Na<sup>+</sup> coordinating PF<sub>6</sub><sup>-</sup> in the first solvation shell is 0, 1, and ≥2, respectively. Figures 3a, S9, and S10 outline the proportions of different solvation structures in each electrolyte and highlight the representative structures in F-P and FFHF-P using ball-and-stick models. In the electrolyte with pure FEC as the solvent, 45.5% of Na<sup>+</sup> tends to stay in the SSIP state, with the remaining 42.4 and 12.1% existing in the CIPs and AGGs, respectively. On the contrary, with the introduction of LCNS, the proportions of CIPs and AGGs increased gradually. In FFHF-P, the Na<sup>+</sup> coordination structures are further transformed into more aggregated structures, and the total proportion of AGGs increases significantly to 34.8%, confirming that the anions are extensively coordinated. Compared to SSIP, such a change toward aggregated states is beneficial for reducing the decomposition of solvents and promotes the formation of anion-derived CEI with abundant inorganic components, thereby improving the stability and ionic transport ability on the interphase. The binding energies between solvents and PF<sub>6</sub><sup>-</sup> were determined by the DFT method to investigate the coupling between the molecule and the anion (Figure S11). Among the selected solvents, TFP has the strongest interaction with PF<sub>6</sub><sup>-</sup>, attributed to its high fluorine content and symmetric molecular structure, which stabilizes the interaction with PF<sub>6</sub><sup>-</sup>. According to the previous report by Chen et al., such a strong interaction can achieve a dragging effect on the anion.<sup>50</sup> Therefore, the addition of TFP

can facilitate the induction of more anions into the solvation structure through the dipole effect while realizing a low solvation effect, which further contributes to the participation of PF<sub>6</sub><sup>-</sup> in film formation. The above results of the simulations prove that the anion-dominated solvation structures have been successfully constructed by modulating the cation-anion interaction (Figure 3b).

The Na<sup>+</sup> solvation structure in electrolytes is not only related to the behavior and properties themselves but also determines the formation of the electrode/electrolyte interphase. Considering that the FFHF-P shows satisfactory electrochemical properties in NIBs, it is critically important to explore the composition and unveil the origin of the CEI formed on the cathode. The CEI on NFMT after 60 cycles was conducted by fitting detailed X-ray photoelectron spectroscopy (XPS) peaks and binding energies. As displayed in the normalized XPS fitting results of C 1s and O 1s spectra (Figures 4a and S12–14), the relatively high intensity of solvent decomposition products (such as C–O and C–H species) can be found in PC-P and F-P, indicating severe degradation of organic solvents. On the contrary, according to the reduced ratio of organic-group signals to the peak at 284.8 eV representing the C–C, the anion-induced solvation structure successfully inhibits solvent decomposition with fewer side reactions in the system. Figure 4b,c shows the high-resolution XPS spectra of the F 1s and P 2p of the CEI layer in PC-P, F-P, and FFHF-P electrolytes. Compared to PC-P, a higher intensity of Na–F peak at 685.1 eV representing the NaF can be detected in F-P, which is owing to the introduction of more F-products by FEC as a donor of F. Notably, the CEI formed in FFHF-P electrolyte develops a distinct high NaF content with a stronger P–O signal, suggesting that the anion-rich solvation structure promotes anionic participation in the evolution of interphase, and leads to more F- and P-containing inorganic byproducts.<sup>51</sup>

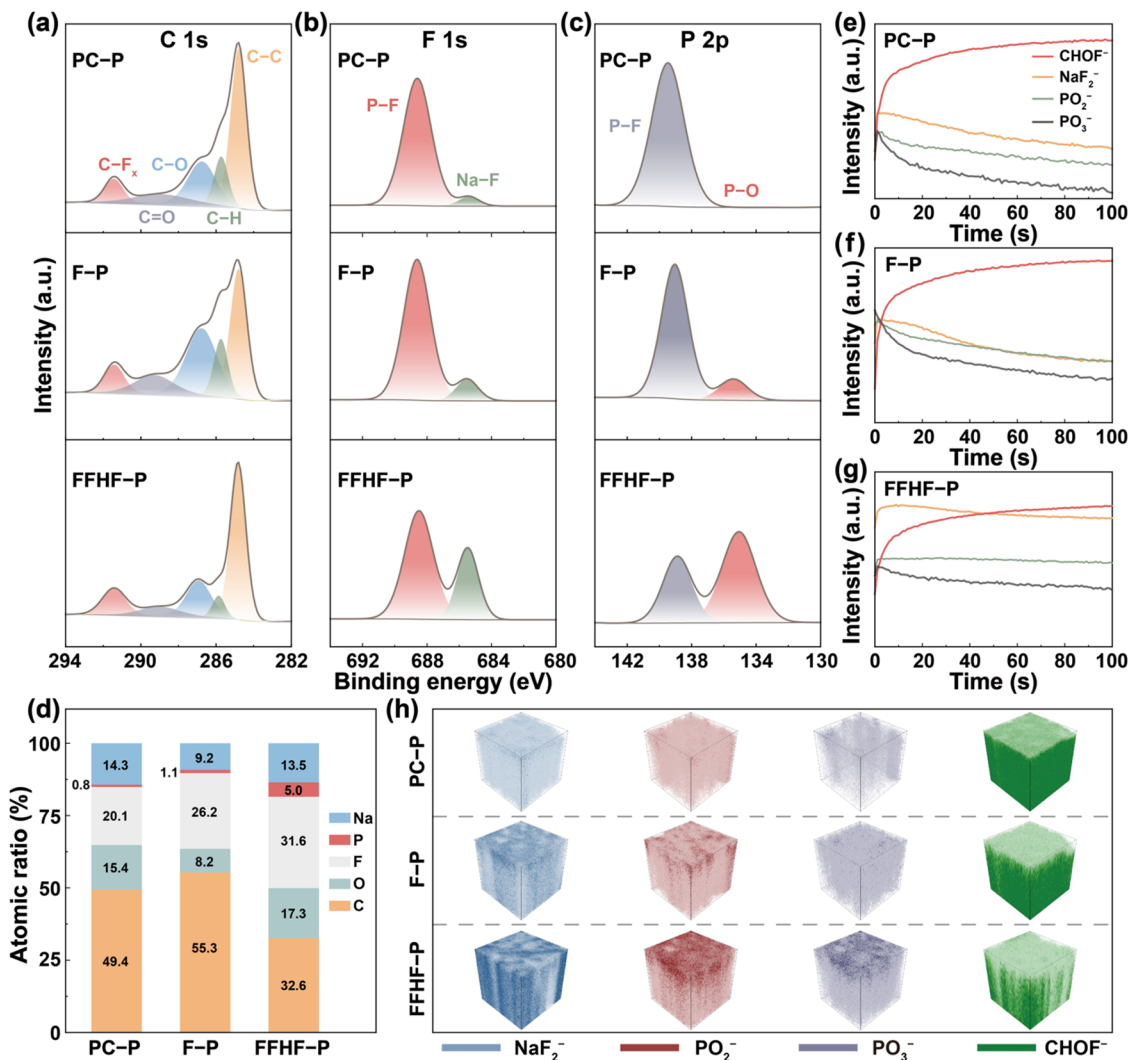


**Figure 4.** (a–c) Normalized XPS fitting curves (C 1s, F 1s, and P 2p) of NFMT cycling in PC-P, F-P, and FFHF-P and (d) the atomic contents derived from XPS spectra. (e–g) Sputtering profiles of selected species in the NFMT cathode using PC-P, F-P, and FFHF-P from the TOF-SIMS tests and (h) the corresponding 3D reconstruction images.

As illustrated in Figure 4d, the anion-dominated film-forming process in FFHF-P contributes to a more stable interphase that contains more F and P-based components.

More details of the spatial distribution of species in the CEI were deeply explored by time-of-flight secondary ion mass spectrometry (TOF-SIMS). The characteristic CHOF<sup>-</sup>, NaF<sub>2</sub><sup>-</sup>, PO<sub>2</sub><sup>-</sup>, and PO<sub>3</sub><sup>-</sup> fragments are selected as primary focus to trace the decomposition products between solvents and PF<sub>6</sub><sup>-</sup>. Figure 4e–g demonstrates the variations in the products from surface to inside in CEI. Clearly, the signal intensities of PO<sub>2</sub><sup>-</sup> and PO<sub>3</sub><sup>-</sup> are much lower in PC-P and F-P systems and decrease sharply with depth. Meanwhile, strong CHOF<sup>-</sup> signals representing organic components appear in both CEI formed in PC-P and F-P, indicating a substantial decomposition of solvents during the film-forming process. In the above XPS results, a relatively high content of fluorinated substances can be found on the cathode cycled in F-P. Further, the TOF-SIMS data illustrate that a large portion of this fluoride is present in the organic state, which is mainly derived from the degradation of fluorinated solvents. This phenomenon can be induced by the strong and dominant Na<sup>+</sup>–FEC interaction discussed in the solvation structure

model. In sharp contrast, the electrode/electrolyte interphase developed in the FFHF-P electrolyte indicates high contents of NaF<sub>2</sub><sup>-</sup>, PO<sub>2</sub><sup>-</sup>, and PO<sub>3</sub><sup>-</sup>, while the lower intensity of the CHOF<sup>-</sup> signal occurs throughout the whole sputtering process. The three-dimensional (3D) rendering region visualizes the distribution and concentration gradient of the selected species in CEI (Figure 4h). As a result, these outcomes convincingly demonstrate that the decomposition of organic solvents is effectively mitigated in the FFHF-P system while the anions undergo a more drastic reaction. Such a process results in the construction of a dense and homogeneous CEI, where stable inorganic components (such as NaF) are evenly distributed, enabling a uniform Na<sup>+</sup> flux and reducing the interfacial polarization. The formation of such interphase is attributed to the stable anion-derived solvation structure in the designed FFHF-P electrolyte, inducing extensive participation of anions in the film formation, consistent with the above analysis. Typically, NaF delivers great electronic insulating properties and is considered an excellent interfacial passivator, which can effectively block electron tunneling through the interfacial layer, suppressing the unfavorable side reactions and constant thickening of CEI.<sup>52,53</sup> Besides, ascribed to its high

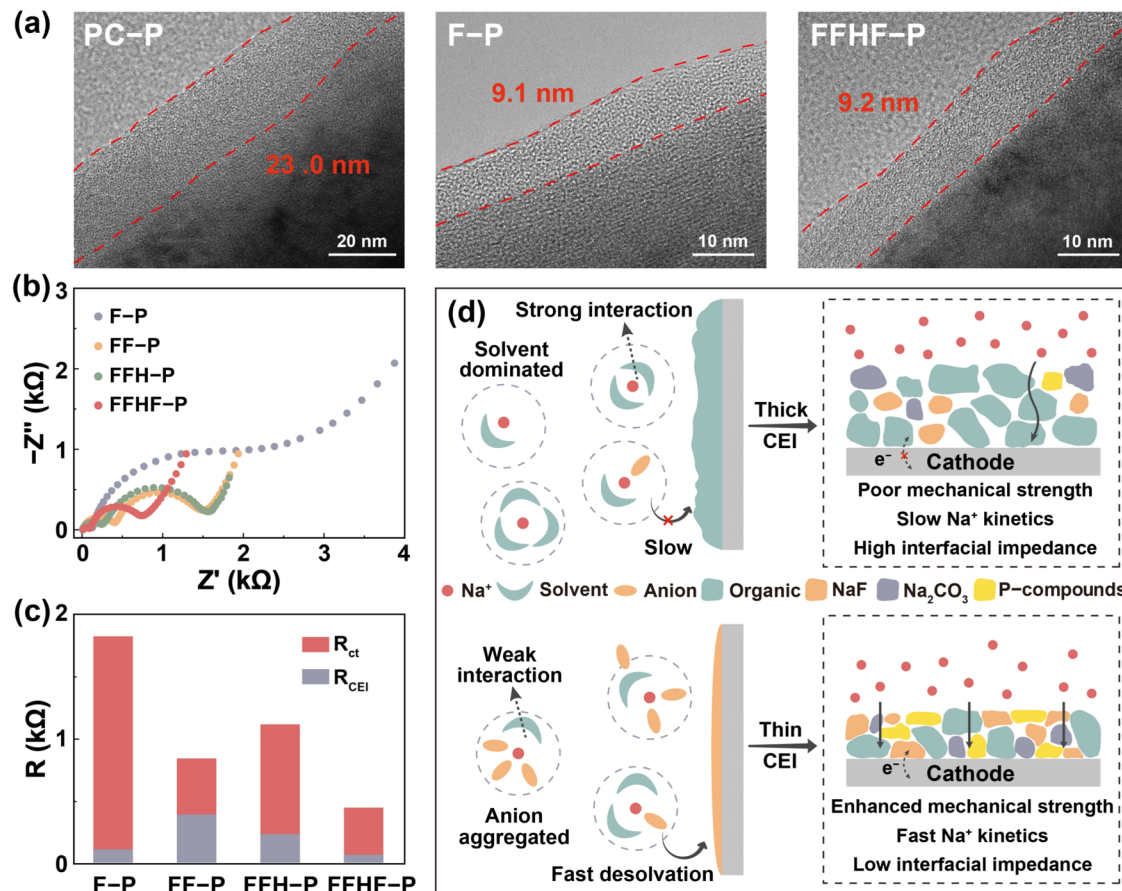


**Figure 5.** (a) High-resolution TEM images of CEI on cycled NFMT. (b) Nyquist plots of NFMT//Na batteries cycled in various electrolytes and (c) the corresponding fitting results. (d) Schematic diagrams of the CEI in different electrolyte systems.

mechanical strength, this NaF-rich structure can greatly endure the volume change behaviors of the cathode at high voltage during charging/discharging.<sup>22,54</sup>

The morphology of CEI on cycled NFMT also corroborates the differences caused by electrolytes (Figure 5a). Electrolytes experience sustained decomposition until a continuous CEI forms on the cathode and blocks the electron transfer. As depicted by transmission electron microscopy (TEM), the thicknesses of the CEI are ~23.0, 9.1, and 9.2 nm in PC-P, F-P, and FFHF-P electrolytes, respectively. The thinner CEI in fluorinated electrolytes means fewer destruction/reconstruction side reactions at high voltage due to the enhanced oxidative stability of F-containing solvents. Further, the impedance of cycled NFMT//Na batteries was measured by EIS, as manifested in Figures 5b and S15. All EIS data were fitted by an equivalent circuit (Figure S16), and the results are listed in Figure 5c and Table S2. Nyquist plots for each electrolyte consist of two semicircles in the high-frequency-region (correlating to Na<sup>+</sup> transport through the interphase and the electrode surface) and a sloping line in the low-frequency region (corresponding to the Na<sup>+</sup> diffusion in bulk). Taken together, the charge transfer resistance ( $R_{ct}$ ) of CEI generated from F-P is still high (1832.4  $\Omega$ ) despite it being thin. Whereas, the NFMT cycled in FFHF-P is not only covered by a thin and uniform CEI but also delivers the minimum  $R_{ct}$  and the lowest interphase impedance ( $R_{CEI}$ ), implying less obstruction to Na<sup>+</sup> diffusion through the interface. Such gaps mainly stem from the different CEI components. Combining the above XPS and TOF-SIMS

results, although exhibiting a thickness similar to the CEI in FFHF-P, the CEI generated in F-P is primarily derived by the solvents. The poor protection ability of such a soft, porous, organic-rich CEI is insufficient to passivate the electrode and survive the permeation of electrolyte, resulting in notorious side reactions. In addition, the higher desolvation energy of F-P also hampers the rapid transport of Na<sup>+</sup>. Conversely, the solvation structure with anion-aggregating in FFHF-P is designed through the cation–anion regulation, thus constructing the NaF-rich CEI on the cathode (Figure 5d). Such a thin, dense, homogeneous, and stable inorganic-rich layer facilitates the separation of electrolyte and electrode and inhibits the parasitic reaction between them, protecting the stability of the cathode during the cycling process. Meanwhile, it promotes the Na<sup>+</sup> migration along the grain boundaries, showing fast transport kinetics, which effectively reduces the interfacial resistance, thus optimizing the electrochemical performance of NIBs.

The electrochemical properties of the designed electrolyte were evaluated by assembling NFMT//Na batteries. The cyclic voltammetry (CV) curves of batteries equipping different electrolytes at 0.1 mV s<sup>-1</sup> are displayed in Figures 6a and S17. It can be observed that the oxidation peak around 3.27 V gradually moves to a lower potential when LCNS is added, manifesting smaller polarization in the designed electrolyte system. Besides, the redox peaks in the FFHF-P are much sharper and overlap better in the subsequent cycles, suggesting improved redox kinetics and reversibility. All cells in different electrolytes illustrate similar initial curves, while the

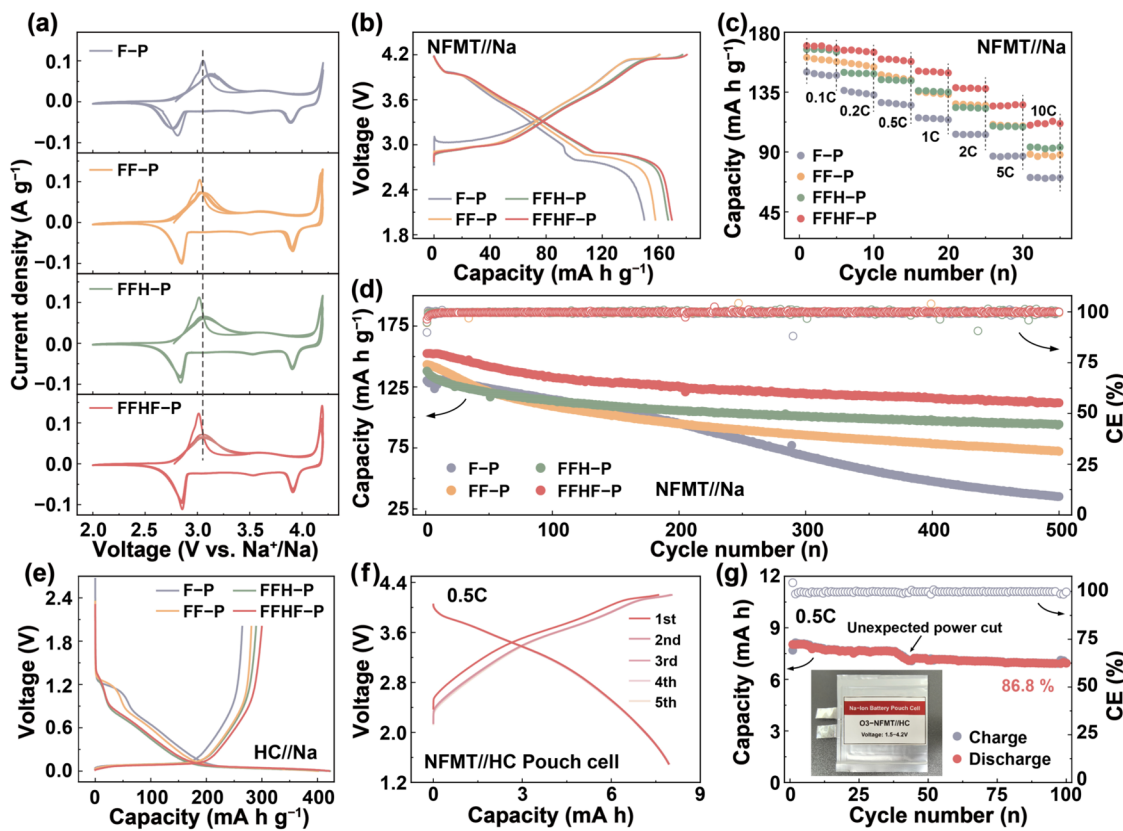


**Figure 6.** (a) CV curves of NFMT//Na cells using F-P, FF-P, FFH-P, and FFHF-P electrolytes with a scan rate of  $0.1 \text{ mV s}^{-1}$  and their (b) initial charge/discharge voltage curves, (c) rate capability, and (d) cycling performance at 1C. (e) First charge/discharge curves of HC//Na batteries in different electrolytes. (f) Charge/discharge curves of NFMT//HC pouch cells with FFHF-P and (g) their cycling performance at 0.5C.

NFMT//Na employing the FFHF-P delivers a discharge capacity of up to  $169.7 \text{ mAh g}^{-1}$ , much higher than batteries with other fluorinated electrolytes and PC-P (Figures 6b and S18). Due to the enhanced oxidative stability and the construction of the special solvation structure with anionic aggregation, FFHF-P underwent less decomposition during the initial cycle and led to the formation of a thin and stable CEI. Consequently, the cells with FFHF-P deliver a higher initial Coulombic efficiency (CE) of 95.1%, while the CE of PC-P and F-P are 91.8 and 92.5%, respectively. When tested at higher rates, as shown in Figures 6c and S19, the NFMT cathode maintains poor reversible capacities of about 70.8 and  $92.5 \text{ mAh g}^{-1}$  at a high rate of 10C after continuous rate cycles in the F-P and PC-P electrolytes. In contrast, a much higher capacity of over  $110.1 \text{ mAh g}^{-1}$  is realized in the FFHF-P system, exhibiting much enhanced rate performance. Such enhanced performance can be attributed to the low desolvation energy of FFHF-P and the inorganic fluoride-rich CEI, as discussed above, which effectively reduce the obstruction of  $\text{Na}^+$  through the interface and decrease the polarization, facilitating the transport of  $\text{Na}^+$  at high current densities. When cycled at a 1C rate, batteries using F-P and PC-P suffer from fast capacity decay, and only 35.1 and  $30.4 \text{ mAh g}^{-1}$  capacity are preserved after 500 cycles, corresponding to poor retentions of 26.9 and 21.5% (Figures 6d and S20). This may be attributed to the severe degradation of solvents, leading to the unstable and high-impedance organic CEI. Although the cycling stability gradually improves after adding the LCNS, the discharge capacities of the batteries in FF-P and FFH-P still decay to 72.1 and  $98.2 \text{ mAh g}^{-1}$ , respectively. As for FFHF-P,

it exhibits greater resistance to deterioration due to the derivation of a robust conductive interphase and its intrinsically high oxidative stability, which can suppress the severe destructive/reconstructive side reactions on the cathode. Consequently, cells with FFHF-P realize a high capacity of up to  $112 \text{ mAh g}^{-1}$  after 500 cycles. In addition, FFHF-P provides a rapid rise in CE within 4 cycles and remains stable with a high average CE value of 99.9%. In comparison, the CE values in PC-P and F-P are both 99.5%, respectively (Figure S21). To explore the application prospects, the electrolytes were tested in NFMT//Na batteries with a larger cathodic loading. As shown in Figures S22–26, the batteries employing FFHF-P still deliver the most stable cycling performance and favorable rate performance. Galvanostatic cycling measurements were also performed in Na//Na symmetrical cells at  $0.2 \text{ mA cm}^{-2}$  with a cycling capacity of  $0.2 \text{ mAh cm}^{-2}$  to verify the advantages of such fluorinated electrolytes for Na metal (Figures S27–32). Among all electrolytes, the overpotential of cells with FFHF-P decreased significantly after several initial cycles of the interfacial activation process and exhibited a stable long-term cycling performance. Na//Na cells with FFHF-P exhibit an overpotential of approximately 0.04 V and low interfacial impedance even after 1600 h. In contrast, large voltage fluctuations and a rapidly increasing overpotential occur in other electrolytes.

In our previous work, a phosphate-based flame-retardant electrolyte was reported to achieve stable cycling in NFMT//Na batteries.<sup>15</sup> However, the intrinsic chemical properties of phosphate esters lead to a bottleneck in their compatibility with carbon-based anodes.<sup>55,56</sup> Hence, its application is limited

to sodium–metal batteries, which fundamentally hinders their use in NIBs and more practical scenarios. Based on this consideration, the compatibility of the designed electrolytes with the HC anode was evaluated. The electrochemical performance of HC//Na batteries was carried out under 0.2C. As displayed in Figures 6e and S33, the HC anodes operated with F-P and FF-P provide high-voltage plateaus during the initial cycle and can only maintain a low capacity, which even decays rapidly. Among all, the HC with FFHF-P delivers a reversible specific capacity over 280 mAh g<sup>-1</sup> and demonstrates the highest capacity retention, indicating great compatibility with the HC anode. Building upon the optimum performance achieved with both NFMT cathode and HC anode, NFMT//HC full cells were assembled. The full cells provide initial discharge capacities of 119.8 and 161.2 mAh g<sup>-1</sup> in F-P and FFHF-P (Figure S34). In the cycling test, cells working in F-P undergo severe capacity fading and polarization increasing upon cycling. On the contrary, NFMT//HC batteries can steadily operate at 0.5C for over 100 cycles and exhibit a high capacity retention of 86.0% in FFHF-P (Figure S35). Also, the better-overlapped profiles also demonstrate the impressive cycling stability of FFHF-P (Figures S36 and S37). As is evident in Figure S38, the rate performance of NFMT//HC was tested at different current densities. The full cells can endure the rapid charge/discharge at 1C rate and maintain a discharge capacity of 138.1 mAh g<sup>-1</sup>. To further verify the feasibility and practical commercial application potential of the designed electrolyte, the NFMT//HC pouch cells were prepared. Figures 6f,g, S39, and S40 present the cycling performance of the pouch cells with FFHF-P at 0.2 and 0.5 C after battery formation. Attributed to its great compatibility of FFHF-P with both NFMT and HC electrodes, the pouch cells deliver great stability with high CE (~99.8%). They maintain 87.5% capacity retention after 50 cycles at 0.2C and 86.8% capacity retention after 100 cycles at 0.5C. Taken together, the FFHF-P electrolyte shows exceptional electrochemical stability compared to other tested electrolytes, confirming it is an ideal candidate for NIBs. These optimized properties are driven by the high antioxidant ability of fluorinated solvents, special aggregated solvation structure, and stable CEI induced by the anions.

## CONCLUSIONS

To summarize, a flame-retardant all-fluorinated electrolyte with high stability and intrinsic safety was rationally designed for NIBs through cation–anion interaction regulation. By introducing LCNS into the FEC solvent, the interionic interactions are significantly enhanced, promoting anion aggregation and forming an anion-derived fluoride-rich CEI layer on the cathode. Such thin, stable, and homogeneous inorganic-rich interphase efficiently suppresses the parasitic reaction, strengthens the interfacial stability, and facilitates fast Na<sup>+</sup> transport kinetics across the interface. As a result, the FFHF-P electrolyte endows the NFMT cathode to achieve a high discharge capacity (169.7 mAh g<sup>-1</sup>), satisfactory rate performance (110.1 mAh g<sup>-1</sup> under 10C rate), and stable cycling ability at 1C for 500 cycles at 4.2 V. More significantly, NFMT//HC pouch cells with such electrolytes exhibit stable operation, retaining 86.8% of capacity after 100 cycles at 0.5C. Besides, the incorporation of this flame-retardant electrolyte significantly endows NIBs with enhanced safety. This work provides promising strategies for regulating the Na<sup>+</sup> solvation structure and interfacial engineering, paving the way for the

practical application of intrinsically safe and high-performance NIBs.

## ASSOCIATED CONTENT

### Supporting Information

The Supporting Information is available free of charge at <https://pubs.acs.org/doi/10.1021/jacs.4c18326>.

Details of electrolyte synthesis, electrode synthesis, characterizations, electrochemical characterization, and theoretical calculations; physicochemical properties of electrolytes, including compositions, calculation results, desolvation energy, and flammability tests; Raman and FTIR results; electrochemical results; XPS results ([PDF](#))

## AUTHOR INFORMATION

### Corresponding Authors

Mengting Liu – Center of Nanomaterials for Renewable Energy, State Key Laboratory of Electrical Insulation and Power Equipment, School of Electrical Engineering, Xi'an Jiaotong University, Xi'an 710049 Shaanxi, P. R. China; Email: liumt39@outlook.com

Hong Zheng – Center of Nanomaterials for Renewable Energy, State Key Laboratory of Electrical Insulation and Power Equipment, School of Electrical Engineering, Xi'an Jiaotong University, Xi'an 710049 Shaanxi, P. R. China;  [orcid.org/0000-0001-5336-9854](https://orcid.org/0000-0001-5336-9854); Email: zhenghong666@xjtu.edu.cn

Xiao Ji – School of Optical and Electronic Information-Wuhan National Laboratory for Optoelectronics, Huazhong University of Science and Technology, Wuhan 430074 Hubei, P. R. China; Email: jixiao@hust.edu.cn

Peng-Fei Wang – Center of Nanomaterials for Renewable Energy, State Key Laboratory of Electrical Insulation and Power Equipment, School of Electrical Engineering, Xi'an Jiaotong University, Xi'an 710049 Shaanxi, P. R. China; Jiangsu Jufeng New Energy Technology Co., Ltd., Changzhou 213166 Jiangsu, P. R. China;  [orcid.org/0000-0001-9882-5059](https://orcid.org/0000-0001-9882-5059); Email: pfwang@xjtu.edu.cn

### Authors

Yi-Hu Feng – Center of Nanomaterials for Renewable Energy, State Key Laboratory of Electrical Insulation and Power Equipment, School of Electrical Engineering, Xi'an Jiaotong University, Xi'an 710049 Shaanxi, P. R. China;  [orcid.org/0000-0002-8323-9361](https://orcid.org/0000-0002-8323-9361)

Chengye Lin – School of Optical and Electronic Information-Wuhan National Laboratory for Optoelectronics, Huazhong University of Science and Technology, Wuhan 430074 Hubei, P. R. China; China-EU Institute for Clean and Renewable Energy, Huazhong University of Science and Technology, Wuhan 430074 Jiangsu, P. R. China

Hanwen Qin – Center of Nanomaterials for Renewable Energy, State Key Laboratory of Electrical Insulation and Power Equipment, School of Electrical Engineering, Xi'an Jiaotong University, Xi'an 710049 Shaanxi, P. R. China

Guang-Xu Wei – Center of Nanomaterials for Renewable Energy, State Key Laboratory of Electrical Insulation and Power Equipment, School of Electrical Engineering, Xi'an Jiaotong University, Xi'an 710049 Shaanxi, P. R. China

Chao Yang – State Key Laboratory of Advanced Technology for Materials Synthesis and Processing, Wuhan University of Technology, Wuhan 430070 Hubei, P. R. China

**Yongwei Tang** — Center of Nanomaterials for Renewable Energy, State Key Laboratory of Electrical Insulation and Power Equipment, School of Electrical Engineering, Xi'an Jiaotong University, Xi'an 710049 Shaanxi, P. R. China

**Xu Zhu** — Center of Nanomaterials for Renewable Energy, State Key Laboratory of Electrical Insulation and Power Equipment, School of Electrical Engineering, Xi'an Jiaotong University, Xi'an 710049 Shaanxi, P. R. China

**Shuai Sun** — Center of Nanomaterials for Renewable Energy, State Key Laboratory of Electrical Insulation and Power Equipment, School of Electrical Engineering, Xi'an Jiaotong University, Xi'an 710049 Shaanxi, P. R. China

**Tian-Ling Chen** — Center of Nanomaterials for Renewable Energy, State Key Laboratory of Electrical Insulation and Power Equipment, School of Electrical Engineering, Xi'an Jiaotong University, Xi'an 710049 Shaanxi, P. R. China

**Ya You** — State Key Laboratory of Advanced Technology for Materials Synthesis and Processing, Wuhan University of Technology, Wuhan 430070 Hubei, P. R. China;  
✉ [orcid.org/0000-0002-2069-5212](https://orcid.org/0000-0002-2069-5212)

Complete contact information is available at:

<https://pubs.acs.org/10.1021/jacs.4c18326>

## Notes

The authors declare no competing financial interest.

## ACKNOWLEDGMENTS

This work was supported by the National Natural Science Foundation of China (Grant Nos. 52472249, 22409161, 52203296), the Young Talent Support Plan of Xi'an Jiaotong University (Grant No. DQ6J011), State Key Laboratory of Electrical Insulation and Power Equipment (Grant No. EIPE23313), and Jiangsu Jufeng New Energy Technology Co., Ltd. (Grant No. 202309227). Prof. P.-F.W. also acknowledges the support from the Young Elite Scientists Sponsorship Program by the Chinese Association for Science and Technology, the "High-Level Talent Introduction Plan" of Shaanxi Province, and the Siyuan Scholar of Xi'an Jiaotong University. The authors acknowledge the help from the Instrument Analysis Center of Xi'an Jiaotong University.

## REFERENCES

- (1) Gabriel, E.; Wang, Z.; Singh, V. V.; Graff, K.; Liu, J.; Koroni, C.; Hou, D.; Schwartz, D.; Li, C.; Liu, J.; Guo, X.; Osti, N. C.; Ong, S. P.; Xiong, H. Influence of Interlayer Cation Ordering on Na Transport in P2-Type  $\text{Na}_{0.67-x}\text{Li}_x\text{Ni}_{0.33-z}\text{Mn}_{0.67+z}\text{O}_2$  for Sodium-Ion Batteries. *J. Am. Chem. Soc.* **2024**, *146*, 15108–15118.
- (2) Wang, Z.; Ni, J.; Li, L. Gradient Designs for Efficient Sodium Batteries. *ACS Energy Lett.* **2022**, *7*, 4106–4117.
- (3) Chen, M.; Hua, W.; Xiao, J.; Zhang, J.; Lau, V. W.-h.; Park, M.; Lee, G.-H.; Lee, S.; Wang, W.; Peng, J.; Fang, L.; Zhou, L.; Chang, C.-K.; Yamauchi, Y.; Chou, S.; Kang, Y.-M. Activating a Multielectron Reaction of NASICON-Structured Cathodes toward High Energy Density for Sodium-Ion Batteries. *J. Am. Chem. Soc.* **2021**, *143*, 18091–18102.
- (4) Ould, D. M. C.; Menkin, S.; Smith, H. E.; Riesgo-Gonzalez, V.; Jónsson, E.; O'Keefe, C. A.; Coowar, F.; Barker, J.; Bond, A. D.; Grey, C. P.; Wright, D. S. Sodium Borates: Expanding the Electrolyte Selection for Sodium-Ion Batteries. *Angew. Chem., Int. Ed.* **2022**, *61*, No. e202202133.
- (5) Gao, Y.; Zhang, H.; Peng, J.; Li, L.; Xiao, Y.; Li, L.; Liu, Y.; Qiao, Y.; Chou, S.-L. A 30-Year Overview of Sodium-Ion Batteries. *Carbon Energy* **2024**, *6*, No. e464.
- (6) Rudola, A.; Sayers, R.; Wright, C. J.; Barker, J. Opportunities for Moderate-Range Electric Vehicles Using Sustainable Sodium-Ion Batteries. *Nat. Energy* **2023**, *8*, 215–218.
- (7) Ma, M.; Chen, B.; Tu, Y.; Pan, H. Ternary Electrolyte Enables High-Voltage and High-Temperature Na-Ion Batteries. *ACS Energy Lett.* **2024**, *9*, 4653–4665.
- (8) Liang, X.; Hwang, J.-Y.; Sun, Y.-K. Practical Cathodes for Sodium-Ion Batteries: Who Will Take the Crown? *Adv. Energy Mater.* **2023**, *13*, No. 2301975.
- (9) Zhang, K.; Xu, Z.; Li, G.; Luo, R.-J.; Ma, C.; Wang, Y.; Zhou, Y.-N.; Xia, Y. Regulating Phase Transition and Oxygen Redox to Achieve Stable High-Voltage O3-Type Cathode Materials for Sodium-Ion Batteries. *Adv. Energy Mater.* **2023**, *13*, No. 2302793.
- (10) Wang, X.-Z.; Zuo, Y.; Qin, Y.; Zhu, X.; Xu, S.-W.; Guo, Y.-J.; Yan, T.; Zhang, L.; Gao, Z.; Yu, L.; Liu, M.; Yin, Y.-X.; Cheng, Y.; Wang, P.-F.; Guo, Y.-G. Fast  $\text{Na}^+$  Kinetics and Suppressed Voltage Hysteresis Enabled by a High-Entropy Strategy for Sodium Oxide Cathodes. *Adv. Mater.* **2024**, *36*, No. 2312300.
- (11) Zhou, Y.; Xu, G.; Lin, J.; Zhang, Y.; Fang, G.; Zhou, J.; Cao, X.; Liang, S. Reversible Multielectron Redox Chemistry in a NASICON-Type Cathode toward High-Energy-Density and Long-Life Sodium-Ion Full Batteries. *Adv. Mater.* **2023**, *35*, No. 2304428.
- (12) Cheng, Z.; Fan, X.-Y.; Yu, L.; Hua, W.; Guo, Y.-J.; Feng, Y.-H.; Ji, F.-D.; Liu, M.; Yin, Y.-X.; Han, X.; Guo, Y.-G.; Wang, P.-F. A Rational Biphasic Tailoring Strategy Enabling High-Performance Layered Cathodes for Sodium-Ion Batteries. *Angew. Chem., Int. Ed.* **2022**, *61*, No. e202117728.
- (13) Cheng, Z.; Zhao, B.; Guo, Y.-J.; Yu, L.; Yuan, B.; Hua, W.; Yin, Y.-X.; Xu, S.; Xiao, B.; Han, X.; Wang, P.-F.; Guo, Y.-G. Mitigating the Large-Volume Phase Transition of P2-Type Cathodes by Synergetic Effect of Multiple Ions for Improved Sodium-Ion Batteries. *Adv. Energy Mater.* **2022**, *12*, No. 2103461.
- (14) Sun, Y.-K. Direction for Commercialization of O3-type Layered Cathodes for Sodium-Ion Batteries. *ACS Energy Lett.* **2020**, *5*, 1278–1280.
- (15) Feng, Y.-H.; Liu, M.; Qi, W.; Liu, H.; Liu, Q.; Yang, C.; Tang, Y.; Zhu, X.; Sun, S.; Li, Y.-M.; Chen, T.-L.; Xiao, B.; Ji, X.; You, Y.; Wang, P.-F. Dual-Anionic Coordination Manipulation Induces Phosphorus and Boron-Rich Gradient Interphase Towards Stable and Safe Sodium Metal Batteries. *Angew. Chem., Int. Ed.* **2025**, *64*, No. e202415644.
- (16) Liu, Q.; Feng, Y.-H.; Zhu, X.; Liu, M.; Yu, L.; Wei, G.-X.; Fan, X.-Y.; Ji, X.; Wang, P.-F.; Xin, H. Stabilizing Cathode-Electrolyte Interphase by Localized High-Concentration Electrolytes for High-Voltage Sodium-Ion Batteries. *Nano Energy* **2024**, *123*, No. 109389.
- (17) Liu, Y.; Zhu, L.; Wang, E.; An, Y.; Liu, Y.; Shen, K.; He, M.; Jia, Y.; Ye, G.; Xiao, Z.; Li, Y.; Pang, Q. Electrolyte Engineering with Tamed Electrode Interphases for High-Voltage Sodium-Ion Batteries. *Adv. Mater.* **2024**, *36*, No. 2310051.
- (18) Wang, X.; Yang, C.; Yao, L.; Wang, Y.; Jiang, N.; Liu, Y. Anion/Cation Solvation Engineering for a Ternary Low-Concentration Electrolyte toward High-Voltage and Long-Life Sodium-Ion Batteries. *Adv. Funct. Mater.* **2024**, *34*, No. 2315007.
- (19) Zhu, C.; Wu, D.; Wang, C.; Ma, J. Flame-Retardant, Self-Purging, High-Voltage Electrolyte for Safe and Long-Cycling Sodium Metal Batteries. *Adv. Funct. Mater.* **2024**, *34*, No. 2406764.
- (20) Zuo, C.; Dong, D.; Wang, H.; Sun, Y.; Lu, Y.-C. Bromide-Based Nonflammable Electrolyte for Safe and Long-Life Sodium Metal Batteries. *Energy Environ. Sci.* **2024**, *17*, 791–799.
- (21) Bates, A. M.; Preger, Y.; Torres-Castro, L.; Harrison, K. L.; Harris, S. J.; Hewson, J. Are Solid-State Batteries Safer Than Lithium-Ion Batteries? *Joule* **2022**, *6*, 742–755.
- (22) Liu, X.; Zheng, X.; Dai, Y.; Wu, W.; Huang, Y.; Fu, H.; Huang, Y.; Luo, W. Fluoride-Rich Solid-Electrolyte-Interface Enabling Stable Sodium Metal Batteries in High-Safe Electrolytes. *Adv. Funct. Mater.* **2021**, *31*, No. 2103522.
- (23) An, K.; Tran, Y. H. T.; Kwak, S.; Han, J.; Song, S.-W. Design of Fire-Resistant Liquid Electrolyte Formulation for Safe and Long-

- Cycled Lithium-Ion Batteries. *Adv. Funct. Mater.* **2021**, *31*, No. 2106102.
- (24) Su, C.-C.; He, M.; Shi, J.; Amine, R.; Yu, Z.; Cheng, L.; Guo, J.; Amine, K. Principle in Developing Novel Fluorinated Sulfone Electrolyte for High Voltage Lithium-Ion Batteries. *Energy Environ. Sci.* **2021**, *14*, 3029–3034.
- (25) Rao, Y.; Li, X.; Zhao, S.; Liu, P.; Wu, F.; Liu, X.; Zhou, N.; Fang, S.; Passerini, S. Fluorinated Electrolyte Formulations Design Enabling High-Voltage and Long-Life Lithium Metal Batteries. *Nano Energy* **2024**, *123*, No. 109362.
- (26) Su, C.-C.; He, M.; Cai, M.; Shi, J.; Amine, R.; Rago, N. D.; Guo, J.; Rojas, T.; Ngo, A. T.; Amine, K. Solvation-Protection-Enabled High-Voltage Electrolyte for Lithium Metal Batteries. *Nano Energy* **2022**, *92*, No. 106720.
- (27) Wang, Y.; Wu, Z.; Azad, F. M.; Zhu, Y.; Wang, L.; Hawker, C. J.; Whittaker, A. K.; Forsyth, M.; Zhang, C. Fluorination in Advanced Battery Design. *Nat. Rev. Mater.* **2024**, *9*, 119–133.
- (28) Zou, Y.; Liu, G.; Wang, Y.; Li, Q.; Ma, Z.; Yin, D.; Liang, Y.; Cao, Z.; Cavallo, L.; Kim, H.; Wang, L.; Alshareef, H. N.; Sun, Y.-K.; Ming, J. Intermolecular Interactions Mediated Nonflammable Electrolyte for High-Voltage Lithium Metal Batteries in Wide Temperature. *Adv. Energy Mater.* **2023**, *13*, No. 2300443.
- (29) Zhang, S.; Li, S.; Wang, X.; Li, C.; Liu, Y.; Cheng, H.; Mao, S.; Wu, Q.; Shen, Z.; Mao, J.; Pan, H.; Lu, Y. Nonflammable Electrolyte with Low Exothermic Design for Safer Lithium-Based Batteries. *Nano Energy* **2023**, *114*, No. 108639.
- (30) Yu, Q.; Xiao, Y.; Zhao, S.; Miao, Y.; Wan, S.; Zhou, L.; Rong, J.; Hou, G.; Chen, S. All-Fluorinated Low-Solvation Electrolytes for High-Voltage Sodium Metal Batteries with Appealing Stability. *Adv. Funct. Mater.* **2024**, *34*, No. 2401868.
- (31) Li, H.; Chen, H.; Shen, X.; Liu, X.; Fang, Y.; Zhong, F.; Ai, X.; Yang, H.; Cao, Y. High-Voltage and Intrinsically Safe Sodium Metal Batteries Enabled by Nonflammable Fluorinated Phosphate Electrolytes. *ACS Appl. Mater. Interfaces* **2022**, *14*, 43387–43396.
- (32) Gao, Y.; Wang, Z.; Tu, H.; Xue, J.; Weng, S.; Lu, S.; Liu, L.; Sun, G.; Peng, K.; Zhang, X.; Li, D.; Liu, Y.; Xu, J.; Li, H.; Wu, X. Low-Temperature and Fast-Charging Sodium Metal Batteries Enabled by Molecular Structure Regulation of Fluorinated Solvents. *Adv. Funct. Mater.* **2025**, *35*, No. 2414652.
- (33) Wu, J.; Tian, Y.; Gao, Y.; Gao, Z.; Meng, Y.; Wang, Y.; Wang, X.; Zhou, D.; Kang, F.; Li, B.; Wang, G. Rational Electrolyte Design toward Cyclability Remedy for Room-Temperature Sodium–Sulfur Batteries. *Angew. Chem., Int. Ed.* **2022**, *61*, No. e202205416.
- (34) Wang, X.; Zhang, C.; Sawczyk, M.; Sun, J.; Yuan, Q.; Chen, F.; Mendes, T. C.; Howlett, P. C.; Fu, C.; Wang, Y.; Tan, X.; Searles, D. J.; Král, P.; Hawker, C. J.; Whittaker, A. K.; Forsyth, M. Ultra-Stable All-Solid-State Sodium Metal Batteries Enabled by Perfluoropolyether-Based Electrolytes. *Nat. Mater.* **2022**, *21*, 1057–1065.
- (35) Jin, Y.; Xu, Y.; Le, P. M. L.; Vo, T. D.; Zhou, Q.; Qi, X.; Engelhard, M. H.; Matthews, B. E.; Jia, H.; Nie, Z.; Niu, C.; Wang, C.; Hu, Y.; Pan, H.; Zhang, J.-G. Highly Reversible Sodium Ion Batteries Enabled by Stable Electrolyte-Electrode Interphases. *ACS Energy Lett.* **2020**, *5*, 3212–3220.
- (36) Wang, S.; Zhang, X.-G.; Gu, Y.; Tang, S.; Fu, Y. An Ultrastable Low-Temperature Na Metal Battery Enabled by Synergy between Weakly Solvating Solvents. *J. Am. Chem. Soc.* **2024**, *146*, 3854–3860.
- (37) Wu, M.; Yang, M.; Yu, J.; Ma, X.; Sun, S.; She, Y.; Yang, J.; Zou, X.; Hu, Y.; Yan, F. Weakly Solvating Electrolytes for Safe and Fast-Charging Sodium Metal Batteries. *J. Am. Chem. Soc.* **2024**, *146*, 35229–35241.
- (38) Sun, C.; Li, R.; Zhu, C.; Chen, L.; Weng, S.; Liu, C.; Deng, T.; Chen, L.; Wang, X.; Fan, X. High-Voltage Li Metal Batteries Enabled by Adsorption-Defluorination Mechanism. *ACS Energy Lett.* **2023**, *8*, 4119–4128.
- (39) Liu, X.; Shen, X.; Luo, L.; Zhong, F.; Ai, X.; Yang, H.; Cao, Y. Designing Advanced Electrolytes for Lithium Secondary Batteries Based on the Coordination Number Rule. *ACS Energy Lett.* **2021**, *6*, 4282–4290.
- (40) Liu, X.; Shen, X.; Li, H.; Li, P.; Luo, L.; Fan, H.; Feng, X.; Chen, W.; Ai, X.; Yang, H.; Cao, Y. Ethylene Carbonate-Free Propylene Carbonate-Based Electrolytes with Excellent Electrochemical Compatibility for Li-Ion Batteries through Engineering Electrolyte Solvation Structure. *Adv. Energy Mater.* **2021**, *11*, No. 2003905.
- (41) Chen, H.; Chen, K.; Yang, J.; Liu, B.; Luo, L.; Li, H.; Chen, L.; Zhao, A.; Liang, X.; Feng, J.; Fang, Y.; Cao, Y. Designing Advanced Electrolytes for High-Safety and Long-Lifetime Sodium-Ion Batteries Via Anion–Cation Interaction Modulation. *J. Am. Chem. Soc.* **2024**, *146*, 15751–15760.
- (42) Lu, Z.; Yang, H.; Yang, Q.-H.; He, P.; Zhou, H. Building a Beyond Concentrated Electrolyte for High-Voltage Anode-Free Rechargeable Sodium Batteries. *Angew. Chem., Int. Ed.* **2022**, *61*, No. e202200410.
- (43) Yao, Y.-X.; Chen, X.; Yan, C.; Zhang, X.-Q.; Cai, W.-L.; Huang, J.-Q.; Zhang, Q. Regulating Interfacial Chemistry in Lithium-Ion Batteries by a Weakly Solvating Electrolyte. *Angew. Chem., Int. Ed.* **2021**, *60*, 4090–4097.
- (44) Ren, H.; Zheng, G.; Li, Y.; Chen, S.; Wang, X.; Zhang, M.; Zhao, W.; Yi, H.; Huang, W.; Fang, J.; Liu, T.; Yang, L.; Liu, M.; Zhao, Q.; Pan, F. Stabilizing LiCoO<sub>2</sub> at 4.6 V by Regulating Anti-Oxidative Solvents. *Energy Environ. Sci.* **2024**, *17*, 7944–7957.
- (45) Zou, Y.; Ma, Z.; Liu, G.; Li, Q.; Yin, D.; Shi, X.; Cao, Z.; Tian, Z.; Kim, H.; Guo, Y.; Sun, C.; Cavallo, L.; Wang, L.; Alshareef, H. N.; Sun, Y.-K.; Ming, J. Non-Flammable Electrolyte Enables High-Voltage and Wide-Temperature Lithium-Ion Batteries with Fast Charging. *Angew. Chem., Int. Ed.* **2023**, *62*, No. e202216189.
- (46) Zou, Y.; Cao, Z.; Zhang, J.; Wahyudi, W.; Wu, Y.; Liu, G.; Li, Q.; Cheng, H.; Zhang, D.; Park, G.-T.; Cavallo, L.; Anthopoulos, T. D.; Wang, L.; Sun, Y.-K.; Ming, J. Interfacial Model Deciphering High-Voltage Electrolytes for High Energy Density, High Safety, and Fast-Charging Lithium-Ion Batteries. *Adv. Mater.* **2021**, *33*, No. 2102964.
- (47) Zhou, X.; Huang, Y.; Wen, B.; Yang, Z.; Hao, Z.; Li, L.; Chou, S.-L.; Li, F. Regulation of Anion-Na<sup>+</sup> Coordination Chemistry in Electrolyte Solvates for Low-Temperature Sodium-Ion Batteries. *Proc. Natl. Acad. Sci. U.S.A.* **2024**, *121*, No. e2316914121.
- (48) Luo, L.; Chen, K.; Cao, R.; Chen, H.; Xia, M.; Zhao, A.; Chen, X.; Chen, W.; Chen, Z.; Fang, Y.; Cao, Y. Ethyl Fluoroacetate with Weak Li<sup>+</sup> Interaction and High Oxidation Resistant Induced Low-Temperature and High-Voltage Graphite//LiCoO<sub>2</sub> Batteries. *Energy Storage Mater.* **2024**, *70*, No. 103438.
- (49) Zhang, W.; Koverga, V.; Liu, S.; Zhou, J.; Wang, J.; Bai, P.; Tan, S.; Dandu, N. K.; Wang, Z.; Chen, F.; Xia, J.; Wan, H.; Zhang, X.; Yang, H.; Lucht, B. L.; Li, A.-M.; Yang, X.-Q.; Hu, E.; Raghavan, S. R.; Ngo, A. T.; Wang, C. Single-Phase Local-High-Concentration Solid Polymer Electrolytes for Lithium-Metal Batteries. *Nat. Energy* **2024**, *9*, 386–400.
- (50) Chen, L.; Chen, M.; Meng, Q.; Zhang, J.; Feng, G.; Ai, X.; Cao, Y.; Chen, Z. Reconstructing Helmholtz Plane Enables Robust F-Rich Interface for Long-Life and High-Safe Sodium-Ion Batteries. *Angew. Chem., Int. Ed.* **2024**, *63*, No. e202407717.
- (51) Kim, S.; Jung, Y.; Park, J.; Hong, M.; Byeon, H. R. Sodium Fluoride-Rich Solid Electrolyte Interphase for Sodium–Metal and Sodium–Oxygen Batteries. *Bull. Korean Chem. Soc.* **2021**, *42*, 1519–1523.
- (52) Zhu, C.; Wu, D.; Wang, Z.; Wang, H.; Liu, J.; Guo, K.; Liu, Q.; Ma, J. Optimizing Naf-Rich Solid Electrolyte Interphase for Stabilizing Sodium Metal Batteries by Electrolyte Additive. *Adv. Funct. Mater.* **2024**, *34*, No. 2214195.
- (53) Zheng, X.; Gu, Z.; Liu, X.; Wang, Z.; Wen, J.; Wu, X.; Luo, W.; Huang, Y. Bridging the Immiscibility of an All-Fluoride Fire Extinguishant with Highly-Fluorinated Electrolytes toward Safe Sodium Metal Batteries. *Energy Environ. Sci.* **2020**, *13*, 1788–1798.
- (54) Zheng, X.; Gu, Z.; Fu, J.; Wang, H.; Ye, X.; Huang, L.; Liu, X.; Wu, X.; Luo, W.; Huang, Y. Knocking Down the Kinetic Barriers Towards Fast-Charging and Low-Temperature Sodium Metal Batteries. *Energy Environ. Sci.* **2021**, *14*, 4936–4947.

(55) Chen, J.; Yang, Z.; Liu, G.; Li, C.; Yi, J.; Fan, M.; Tan, H.; Lu, Z.; Yang, C. Reinforcing Concentrated Phosphate Electrolytes with In-Situ Polymerized Skeletons for Robust Quasi-Solid Lithium Metal Batteries. *Energy Storage Mater.* **2020**, *25*, 305–312.

(56) Zeng, Z.; Murugesan, V.; Han, K. S.; Jiang, X.; Cao, Y.; Xiao, L.; Ai, X.; Yang, H.; Zhang, J.-G.; Sushko, M. L.; Liu, J. Non-Flammable Electrolytes with High Salt-to-Solvent Ratios for Li-Ion and Li-Metal Batteries. *Nat. Energy* **2018**, *3*, 674–681.